

Chemical Science

rsc.li/chemical-science



ISSN 2041-6539



Cite this: *Chem. Sci.*, 2021, **12**, 6879

All publication charges for this article have been paid for by the Royal Society of Chemistry

Reaction-based machine learning representations for predicting the enantioselectivity of organocatalysts†

Simone Gallarati, ^{‡a} Raimon Fabregat, ^{‡a} Rubén Laplaza, ^{ab} Sinjini Bhattacharjee, ^{ac} Matthew D. Wodrich ^{ab} and Clemence Corminboeuf ^{*abd}

Hundreds of catalytic methods are developed each year to meet the demand for high-purity chiral compounds. The computational design of enantioselective organocatalysts remains a significant challenge, as catalysts are typically discovered through experimental screening. Recent advances in combining quantum chemical computations and machine learning (ML) hold great potential to propel the next leap forward in asymmetric catalysis. Within the context of quantum chemical machine learning (QML, or atomistic ML), the ML representations used to encode the three-dimensional structure of molecules and evaluate their similarity cannot easily capture the subtle energy differences that govern enantioselectivity. Here, we present a general strategy for improving molecular representations within an atomistic machine learning model to predict the DFT-computed enantiomeric excess of asymmetric propargylation organocatalysts solely from the structure of catalytic cycle intermediates. Mean absolute errors as low as 0.25 kcal mol⁻¹ were achieved in predictions of the activation energy with respect to DFT computations. By virtue of its design, this strategy is generalisable to other ML models, to experimental data and to any catalytic asymmetric reaction, enabling the rapid screening of structurally diverse organocatalysts from available structural information.

Received 26th January 2021
Accepted 1st April 2021

DOI: 10.1039/d1sc00482d
rsc.li/chemical-science

Introduction

Society's growing need for pharmaceuticals, agricultural chemicals, and materials requires a continuous push in the development of asymmetric catalytic methods.^{1,2} In particular, enantioselective organocatalysis has emerged as a powerful strategy for the stereocontrolled assembly of structurally diverse molecules^{3–5} with constant effort placed in making chemical transformations more selective, efficient, or generally applicable.⁶ Although the computational design of highly selective catalysts has long been viewed as a "Holy Grail" in chemistry,^{7,8} it is generally still more efficient to experimentally screen

a range of potential organocatalysts for a given reaction than to assess their performance *in silico*.⁹ That is because e.e. (enantiomeric excess) values, estimated as the ratio between the competitive reaction rates leading to the two enantiomeric products,¹⁰ are relatively computationally expensive and challenging to predict accurately with standard electronic structure computations. The energy difference between the transition states (TSs) leading to the major and minor enantiomers can be quite small (<2 kcal mol⁻¹) and multiple diastereomeric transition states, stemming from the large conformational space of flexible organocatalysts, can yield the same enantiomer.^{7,11} As the relation between rate constants and computed selectivity is exponential, minor errors in computed energies can lead to major errors in stereochemical outcome prediction. These factors pose a monumental challenge for traditional quantum mechanical (QM) methods, in terms of both accuracy and cost,^{12,13} especially if many conformers and substrate-catalyst combinations have to be computed. While the intrinsic error of the quantum chemical level is often addressed in comprehensive benchmark studies,^{10,14–17} automated toolkits,^{18,19} such as AARON²⁰ and CatVS,²¹ have been developed to streamline the tedious and error-prone task of optimising hundreds of thermodynamically accessible stereocontrolling transition states. Starting from user-defined libraries, multiple conformations and configurations of TS structures are located and optimised.

^aLaboratory for Computational Molecular Design, Institute of Chemical Sciences and Engineering, Ecole Polytechnique Fédérale de Lausanne (EPFL), 1015 Lausanne, Switzerland. E-mail: clemence.corminboeuf@epfl.ch

^bNational Center for Competence in Research-Catalysis (NCCR-Catalysis), Ecole Polytechnique Fédérale de Lausanne (EPFL), 1015 Lausanne, Switzerland

^cIndian Institute of Science Education and Research, Dr Homi Bhabha Rd, Ward No. 8, NCL Colony, Pashan, Pune, Maharashtra 411008, India

^dNational Center for Computational Design and Discovery of Novel Materials (MARVEL), Ecole Polytechnique Fédérale de Lausanne (EPFL), 1015 Lausanne, Switzerland

† Electronic supplementary information (ESI) available. See DOI: 10.1039/d1sc00482d

‡ These authors contributed equally to this work.



Although such accelerated prediction of selectivity is enticing for the prospect of computational catalyst design,⁹ the applicability of QM-based tools such as AARON remains limited either by the cost of the quantum mechanical computations, which quickly become prohibitive, or by the inherent difficulty of locating all transition state structures. On the other hand, tools using QM-derived molecular mechanics force fields (Q2MM), like CatVS, require the development of an MM force field for each new reaction type considered, a major limitation to their widespread application.¹¹

An alternative approach pioneered by Norrby²² and Pradhan²³ and popularised by Sigman and co-workers is to fit experimental reaction outcomes to computationally- and experimentally-derived physical organic molecular descriptors.^{24–26} The difference in free energies at the stereocontrolling transition states²⁷ can be expressed as a polynomial function of global or local steric and electronic parameters, such as Sterimol values, natural bond orbital charges, IR frequencies, HOMO/LUMO energies, and polarisabilities.^{28–34} In principle, the resulting statistical model allows for extrapolation to out-of-sample examples,^{35,36} however, like all QSSR-type methods,³⁷ such multivariate linear regressions are not easily transferable and most suitable only for closely related analogues of the training set, given that a set of appropriate molecular descriptors must be redefined for every new regression.²¹

Nonlinear regression models (e.g., artificial neural networks, random forest, kernel methods)³⁸ have demonstrated the potential to overcome some of the previous limits in catalyst screening and constitute an alternative to multilinear regressions with parameters derived from chemical knowledge and mechanistic hypotheses (e.g., Hammett constants, Tolman cone angles, percent buried volume, vibrational frequencies, pK_a values).^{39–45} Recently, the organic synthetic community has exploited these artificial intelligence-based approaches for predicting $\Delta\Delta G^\ddagger$,²⁷ e.e., the activation energy, the product distribution, or the yield of (asymmetric) catalytic reactions. These models rely on the identification of a large set of system-specific molecular descriptors (e.g., physical organic descriptors like Charton or Sterimol values, NBO charges, NMR chemical shifts, bond distances and angles, HOMO-LUMO gaps, local electro/nucleophilicity, or RDKit descriptors⁴⁶) used as the input from which an algorithm can “learn” while being “supervised” by the reaction outcome (output, *i.e.* $\Delta\Delta G^\ddagger$, e.e., or yield).^{47–62} While the reaction outcome is often obtained from experiment (*i.e.*, phenomenological models), alternatives based on computed data are highly valuable as well.^{63–67} Indeed, so-called quantum (or atomistic) ML models, which map a three-dimensional molecular structure (called molecular representations, *e.g.* CM,⁶⁸ SLATM,⁶⁹ SOAP⁷⁰) to a representative target computed quantum chemically, constitute an appealing complementary strategy owing to its broad applicability and dependence on the laws of physics.^{69,71,72} While these approaches provide a favourable combination of efficiency, scalability, accuracy, and transferability for predicting energetic and more complex molecular properties,⁷¹ identifying enantioselective organocatalysts requires precise predictions of the relative energy barriers for the stereocontrolling

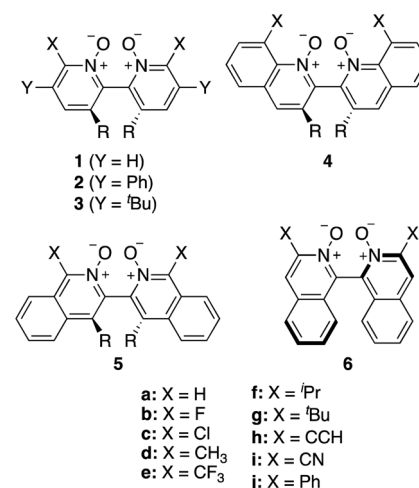
transition states, a target currently beyond their accuracy. Recently, SOAP features of isolated reactants were used to train a machine learning classifier and predict transition state barriers of regioselective arene C–H functionalization. In this work, a large number of molecular fingerprints were combined with the SOAP features to improve the regression, and the resulting model was outperformed in out-of-sample predictions by a random forest model using chemical descriptors with physical organic basis (PhysOrg).⁷³

Here, we provide a stepwise route to improve such QML approaches to reach sufficient accuracy for subtle properties such as those associated with asymmetric catalysis (*i.e.*, e.e.). This objective is achieved by rationally designing a reaction-based representation (*vide infra*) that is a more faithful fingerprint of the enantiodetermining TS energy. The performance of the approach is demonstrated through accurately predicting the DFT-computed enantiomeric excess of Lewis base-catalysed propargylation reactions directly from the structure of the catalytic cycle intermediates. Unlike other ML models trained on (absolute) experimental e.e.’s,^{35,36} our model is able to predict the absolute configuration of the excess product, because it is trained on the activation energy of the enantiodetermining step for each pair of enantiomers (pro-(*R*) and pro-(*S*) intermediates) independently.

Methods

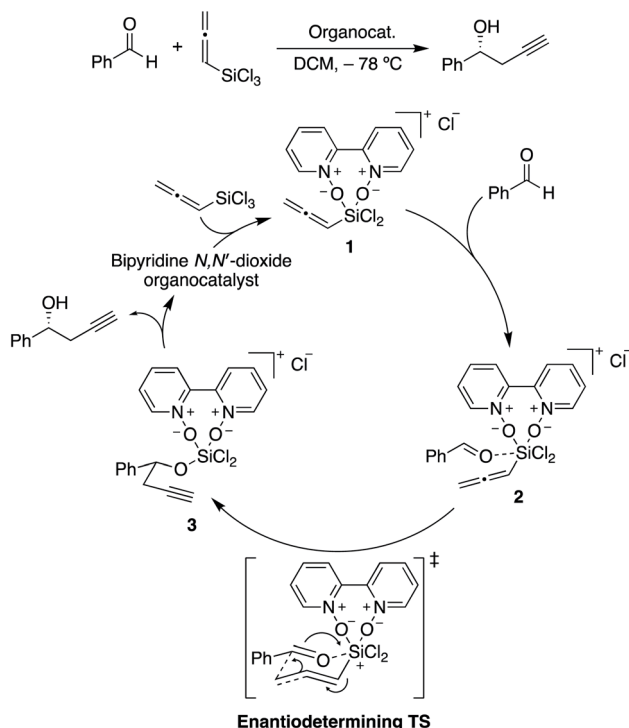
Reaction and organocatalysts database

Asymmetric allylations^{75–78} and propargylations⁷⁹ of aromatic aldehydes are key C–C bond forming transformations, providing access to optically enriched homoallylic and homo-propargylic alcohols, respectively, which serve as valuable building blocks for the synthesis of complex chiral molecules.⁸⁰ Catalysts that are selective for allylations are generally not highly stereoselective for propargylations, which has led to a dearth of stereoselective propargylation catalysts.^{81–85} Tools to screen dozens of allylation catalysts to find promising



Scheme 1 Library of axially chiral bipyridine *N,N'*-dioxide organocatalysts. R = H or Me. Adapted from ref. 74.





Scheme 2 Catalytic cycle for the propargylation of benzaldehyde with allenyltrichlorosilane, showing the rate-limiting and stereocontrolling transition state. Adapted from ref. 85.

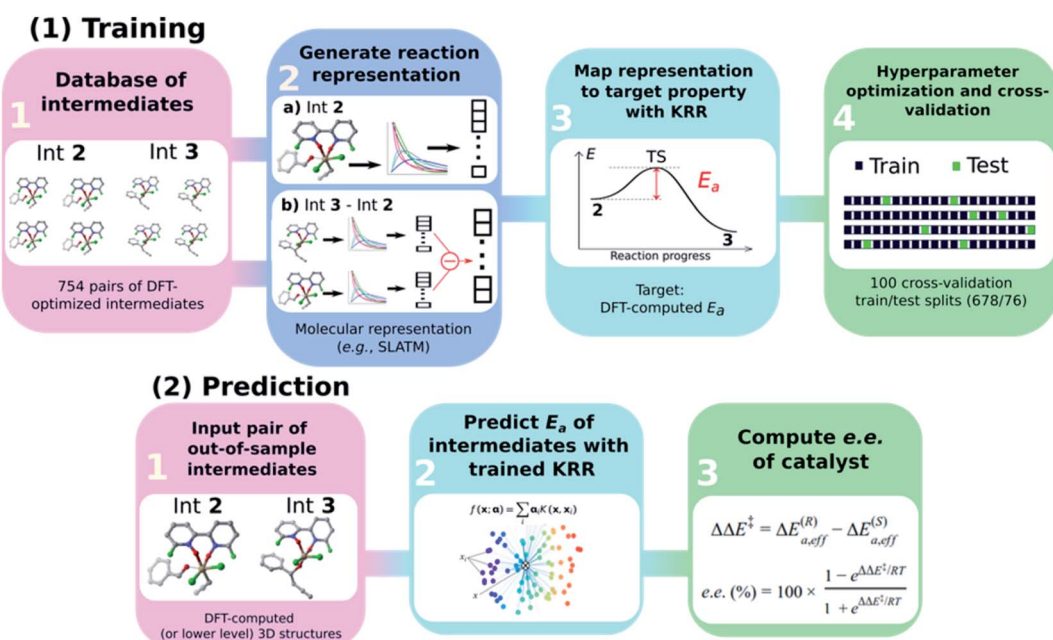
candidates for propargylation reactions are therefore highly valuable.⁹ To this end, Wheeler and co-workers have investigated 76 Lewis base organocatalysts (Scheme 1)⁷⁴ and used the computational toolkit AARON²⁰ to build a database of 760 stereocontrolling transition states to predict their

enantioselectivity in the propargylation of benzaldehyde (Scheme 2).^{14,74,86} Large databases of kinetic data for asymmetric catalysis generated *in silico* are scarce.⁶³ Therefore, this library constitutes an ideal training and validation set for the development of an atomistic ML model with reaction-based representations capable of predicting the e.e. of organocatalysts readily from the structures of intermediates. Note that the workflow presented below would improve the ML performance independently of the size of the training data. The target of the ML model is the DFT-computed relative forward activation energy (E_a , *i.e.*, the energy difference between the TS and the preceding intermediate) associated with each of the 10 (*R*)- or (*S*)-ligand arrangements (see Fig. S1†) of the enantiodetermining TS in Scheme 2 for the 76 catalysts in Scheme 1 (11 catalysts of type 1, 16 of type 2, 15 3, 11 4, 13 5, and 10 catalysts of type 6), yielding a total of 754 E_a values.⁸⁷ e.e. values are computed from E_a (*vide infra*), thus accurate predictions of E_a lead to accurate e.e. predictions.

General ML workflow

The general workflow exploited and improved herein relies on a physics-based ML model for the prediction of the e.e. of the asymmetric catalytic reactions, as illustrated in Scheme 3 and described hereafter. It comprises two parts: part (1) is a training procedure that relies on the following steps:

(1) Database construction: a library of 3D geometries and energies of catalytic cycle intermediates is curated. Here, the structures of 754 pairs of intermediates 2 and 3 are optimised with DFT (see the next section) and used to train the ML model. As shown in our previous work,⁴³ accurate geometries are not necessarily needed as inputs for atomistic ML models; thus, rough-coordinate estimates (*e.g.*, obtained directly from SMILES



Scheme 3 Graphical overview of the workflow used to build an atomistic ML model for e.e. prediction.

strings) or low-cost DFTB structures could potentially be used to generate suitable molecular representations.

(2) Generation of molecular representations: information intrinsically contained within the 3D structure of each intermediate is transformed into a suitable molecular representation. Here we build different variants based on the Spectral London and Axilrod-Teller-Muto (SLATM)⁶⁹ representation. SLATM is composed of two- and three-body potentials, which are derived from the atomic coordinates and contain most of the relevant information to predict molecular properties.^{70,88-94}

(3) Training of the model: input representations are mapped onto the corresponding target values (E_a , computed at the DFT level, see the next section) using Kernel Ridge Regression (KRR)⁹⁵ with a Gaussian kernel. Note that even if target values based on DFT are used here to train the ML model, the strategy proposed hereafter is expected to perform equally well on experimental or more accurate quantum chemical data.

(4) Hyperparameter optimisation and cross-validation: the full dataset is split randomly 100 times into 90/10 training/test sets (678/76 datapoints) to optimise the KRR hyperparameters and obtain the learning curves.

In part (2), the trained ML model is used to predict the activation energy of out-of-sample organocatalysts. The model requires as input the 3D structures of **2** and **3** and delivers the corresponding E_a value. Using the energy of **2** as reference, the relative energies of the enantiodetermining (*R*)- and (*S*)-TSs can be calculated, and the e.e. of the catalyst under investigation computed (*vide infra*).

Computational details

Quantum chemistry

Catalytic cycle intermediates **2** and **3** were optimised at the B97-D/TZV(2p,2d) level of theory,⁹⁶⁻⁹⁸ accounting for solvent effects (dichloromethane, $\epsilon = 8.93$) using the polarizable continuum model (PCM)⁹⁹⁻¹⁰¹ with Gaussian16,^{102,103} in analogy with the study by Wheeler and co-workers.⁷⁴ Density fitting techniques were used throughout. The structures of 1508 intermediates were obtained *via* intrinsic reaction coordinate calculations (IRC)¹⁰⁴ from the TS database curated by Wheeler *et al.*⁷⁴ 754 target E_a values (11 catalysts of type **1**, 16 type **2**, 15 **3**, 11 **4**, 13 **5**, and 10 of type **6**, each in 5 distinct pro-*(R*) and pro-*(S)* ligand arrangements)⁸⁷ were computed (relative to the lowest-lying intermediate **2** ligand arrangement) at the same level, which was shown to provide the best compromise between accurate predictions of low-lying TS energies and stereoselectivities for allylation and propargylation reactions.¹⁴ e.e. values were not predicted from Gibbs free energy barriers, but rather from relative energy barriers (*i.e.*, electronic energies plus solvation free energies), since they have been found to be more reliable than those based on either relative enthalpies or free energy barriers for this reaction.¹⁴ The symbol E_a was therefore used to indicate the energy (electronic plus solvation) difference between the TS and the preceding intermediate. For each C_2 -symmetric catalyst (Scheme 1), 10 distinct ligand arrangements around a hexacoordinate Si centre are possible (**BP1-5**, (*R*)- and (*S*)-, Fig. S1†).⁸⁴⁻⁸⁶ Since each of these can lead to

thermodynamically accessible reaction pathways, and the stereoselectivity is largely a consequence of which ligand arrangement is low-lying for a particular catalyst, all diastereomeric TSs were considered viable and the e.e. calculated from a Boltzmann weighting of the relative energy barriers.⁷⁴ In eqn (1)–(3), $\Delta E_{a,\text{eff}}$ is the relative Boltzmann-weighted activation energy of each (*R*)- or (*S*)-species, $\Delta\Delta E^\ddagger$ is the difference between the (*R*)- and (*S*)-Boltzmann-weighted activation energies, R is the ideal gas constant, and T is the propargylation reaction temperature (195 K).

$$\Delta E_{a,\text{eff}} = -RT \ln \left(\sum_i^{\text{BPi}} e^{-(E_a^{\text{BPi}}/RT)} \right) \quad (1)$$

$$\Delta\Delta E^\ddagger = \Delta E_{a,\text{eff}}^{(R)} - \Delta E_{a,\text{eff}}^{(S)} \quad (2)$$

$$\text{e.e. (\%)} = 100 \times (1 - e^{\Delta\Delta E^\ddagger/RT}) / (1 + e^{\Delta\Delta E^\ddagger/RT}) \quad (3)$$

Machine learning

The Python package QML¹⁰⁵ was used to construct standard SLATM representations. Feature selection and the construction of the reaction-based representations SLATM_{DIFF} and SLATM_{DIFF+} were done using the Python package Scikit-learn.¹⁰⁶ To generate the learning curves and the e.e. predictions, a cross-validation scheme was used with 100 different 90/10 training/test sets (678/76). The KRR hyperparameters (the width of the Gaussian kernel σ and the ridge regularization λ) were optimised for each train/test split, systematically obtaining essentially the same results for each split (see the ESI†). From the 100 train/test splits, the E_a of each intermediate pair (**2** and **3**) was predicted approximately 10 times; these test predictions were then averaged to obtain one final prediction. The standard deviation from the ~10 test predictions were used to generate the error bars. The final average prediction of the E_a value was used to calculate the Boltzmann-weighted $\Delta E_{a,\text{eff}}$ values (eqn (1)) and the $\Delta\Delta E^\ddagger$ of each (*R*)- and (*S*)-pair (eqn (2)), and so the e.e. value of each organocatalyst (eqn (3)). The out-of-sample predictions were done with the same SLATM_{DIFF+} models trained in the cross-validation scheme. Additionally, out-of-sample predictions were done re-training the model on the entire dataset (see Fig. S6†), although this did not lead to noticeable improvement. While simpler representations (*e.g.*, CM,⁶⁸ BoB¹⁰⁷) were tested, SLATM performs significantly better (see Fig. S2†).

Results and discussion

Molecular representations

The key step of the workflow presented above is generating a molecular representation, which is mapped onto the target value (*i.e.*, the activation energy E_a) and used as a fingerprint of the enantiodetermining TS. Representations can be constructed from single molecules and more recently as “ensemble representations”: instead of associating one fixed configuration of

atoms to a single-point geometry energetic target value, information from multiple structures can be combined to generate a representation for an ensemble property, such as the free energy of solvation (ΔG_{sol}).¹⁰⁸ This has recently been achieved by calculating the ensemble average of the FCHL19 representations^{109,110} of a set of configurational snapshots obtained through MD sampling.¹⁰⁸ Here, we propose an alternative approach that goes beyond standard QML representations (*i.e.*, KRR using one given gas-phase geometry)¹⁰⁸ by describing the chemical transformation occurring during the enantiodetermining step of an asymmetric reaction through the comparison of the representations of the two catalytic cycle intermediates preceding and following the stereocontrolling TS. This allows us to generate a “reaction-based” representation, which can be closely mapped to the activation energy of the enantiodetermining step, as discussed later. We rely on “dissimilarity” plots as a diagnostic tool to determine whether a particular representation can adequately characterize the stereocontrolling step. By dissimilarity plots, we refer to histograms of the Euclidean distance between any two representations *vs.* the difference in their target property, which in this case is E_a . For a particular representation to be effective, small distances between structures must correspond to small differences between target properties, as the Euclidean distance is used to measure the similarity of two molecular representations. Similar plots have previously been exploited to analyse the behaviour of molecular representations,^{70,111} but only parenthetically. Here, we highlight their importance as a fundamental analytical tool to understand the performance of molecular representations in kernel methods for asymmetric catalysis and demonstrate their utility for constructing reliable ML models.

Before discussing our proposed representation variants, we report in Fig. 1a the performance of the standard SLATM representation using the structure of a single intermediate (*e.g.*, 2). Due to the structural similarities between 2 and the enantiodetermining TS (in both, the Si atom has 6 coordination sites

occupied, whereas the coordination number is only 5 or 4 in intermediate 3), intermediate 2 was first chosen to construct the input representation. The learning curve for the prediction of E_a using SLATM (blue) of intermediate 2 (denoted SLATM₂) reaches a Mean Absolute Error (MAE) of $0.54 \pm 0.06 \text{ kcal mol}^{-1}$ for the prediction of E_a with 90% of the data used for training (*i.e.*, 680 structures). Considering the exponential relationship between relative activation energies and e.e. values, which implies a dramatic propagation of errors, the accuracy of this approach is insufficient. This is further demonstrated in Fig. 2, which shows the correlation between the predicted and reference $\Delta\Delta E^\ddagger$ values (MAE = $0.96 \text{ kcal mol}^{-1}$), and in Fig. 3, where the e.e. values obtained from SLATM₂ are compared to the

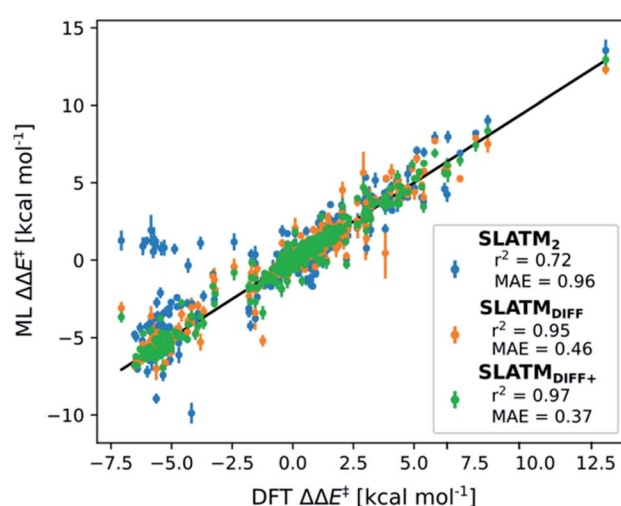


Fig. 2 Predictions of $\Delta\Delta E^\ddagger$ vs. DFT reference for the three approaches discussed. Mean Absolute Errors (MAE) are reported in kcal mol^{-1} . These predictions are obtained by averaging the predictions obtained from the cross-validation scheme with 100 different random train/test splits. The error bars indicate the standard deviation of ML $\Delta\Delta E^\ddagger$, derived from the standard deviations in the E_a prediction of the 100 different random train/test splits.

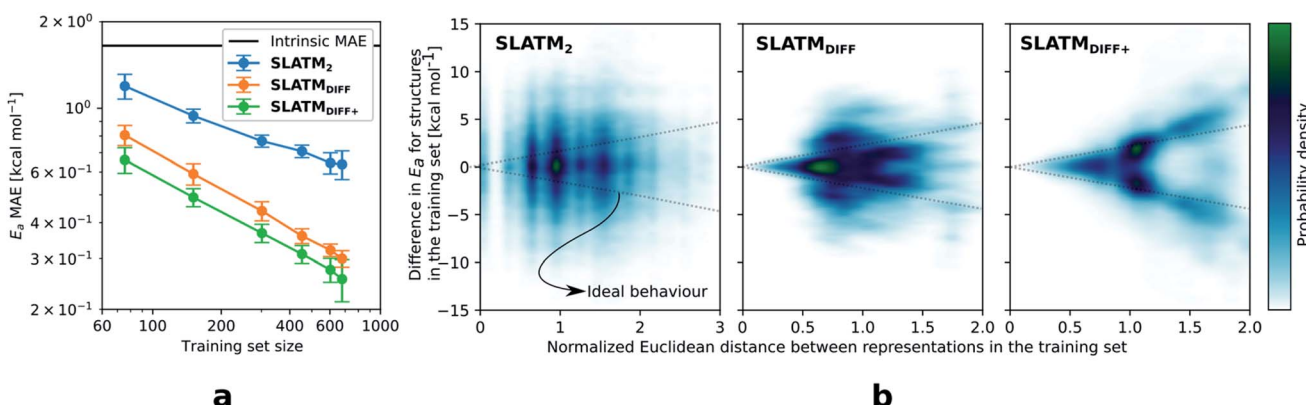


Fig. 1 (a) Learning curves with MAE in test sets predictions of E_a for the three approaches discussed. The error bars correspond to the standard deviations and are computed from the results of 100 different random train/test splits. (b) Dissimilarity plots *i.e.*, difference in target values (E_a) *vs.* Euclidean distance between representations for each pair of points in the dataset (the Euclidean distances have been divided by the average distance between points). When the difference in E_a values tends to zero, the corresponding points should lie in the area delimited by the two dotted straight lines (ideal behaviour).



DFT reference

	1	2	3	4	5	6
a (<i>R</i> = Me)	69	43	67	55	75	
a	76	43	53	25	78	73
b (<i>R</i> = Me)		98	98			
b	89	97	97	71	90	89
c (<i>R</i> = Me)		97	97			
c	91	97	97	76	92	91
d	64	77	83	-47	79	58
e (<i>R</i> = Me)		99	96			
e	94	99	97	18	96	96
f	-36	-13	89	-29	86	62
g	20	-19		75	46	-34
h (<i>R</i> = Me)		99	97			
h	87	98	97	53	92	91
i (<i>R</i> = Me)		91	99			
i	93	95	99	88	96	94
j	44	91	-97	86	48	88

SLATM₂

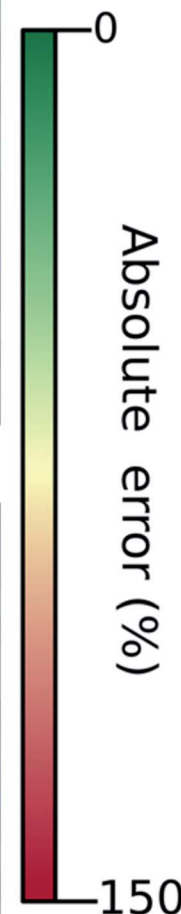
	1	2	3	4	5	6
-72	-28	3	-93	-12		
-73	-32	48	-98	-54	-58	
92	93					
97	83	93	81	81		
78	88					
61	85	91	77	70	90	
-52	-50	31	-61	39	-62	
45	98	93	87	92	81	
85	27	78	-66	89	25	
16	-54		-90	-55	-4	
96	96					
80	85	95	75	87	90	
91	98					
73	99	98	93	95	98	
0	61	-14	93	-45	81	

SLATM_{DIFF}

	1	2	3	4	5	6
24	22	84	58	59		
57	53	87	-11	88	49	
98	98					
95	96	97	73	91	89	
87	98					
79	99	95	89	92	94	
57	75	83	-53	64	60	
87	97		78			
63	99	97	60	99	87	
20	52	23	-49	89	90	
57	35		88	-23	10	
99	99					
91	91	96	61	94	93	
79	96		97			
69	99		98	85	98	
76	77	-23	99	13	84	

SLATM_{DIFF+}

	1	2	3	4	5	6
37	25	74	59	39		
66	22	69	23	89	54	
99	99					
93	94	98	75	89	93	
95	96					
90	97	98	71	86	96	
44	59	91	18	57	59	
99	98					
91	99	97	69	94	86	
-2	-23	41	-2	83	79	
61	21		56	-53	0	
99	98					
94	97	95	8	92	97	
87	99					
85	89	99	95	87	94	
64	78	-82	96	31	89	



Absolute error (%)

Fig. 3 e.e. values obtained from DFT computations (top left) and from the ML predictions of E_a using the three approaches discussed. These predictions are obtained by averaging the predictions obtained from the cross-validation scheme with 100 different random train/test splits. Cells are coloured according to their accuracy with respect to the reference, ranging from dark green (best) to dark red (worst). Positive e.e. values correspond to excess (*R*)-alcohol formation, negative values to excess (*S*)-alcohol formation.

reference quantities: the large number of red-coloured cells indicates large deviations between ML-predicted and DFT-computed e.e. values. The rather poor mapping between SLATM₂ and the E_a of the stereocontrolling step (associated with the key **2** \rightarrow **3** transition state) is evident from the visual inspection of Fig. 3, where the large number of red-coloured cells associated with catalysts bearing substituents **a**, **d**, **e**, **g**, **f** and **j** indicates inaccurate predictions of e.e. values, and from the analysis of the corresponding dissimilarity plot in Fig. 1b (left). In the latter, the large scattering of points lying outside the area delimited by the dotted lines, particularly when the Euclidean distance tends to zero, means that two different structures might be considered equal by the kernel (distance \approx 0) albeit leading to very different E_a values. Thus, the shape of the dissimilarity plot of SLATM₂ deviates considerably from ideal one, indicated by the dotted straight lines.⁷⁰ Note that the MAE for E_a increases up to 0.77 ± 0.05 kcal mol⁻¹ (see Fig. S2†)

if starting from the SLATM representation of **3**, the intermediate following the enantiodetermining step in the catalytic cycle (Scheme 2). The higher accuracy achieved using the representation of **2** vs. **3** could be attributed to the reaction step being exergonic and, according to the Hammond Postulate,¹¹² the enantiodetermining TS resembling **2** more closely. In any case, neither the structure of **2** or **3** provides sufficiently good fingerprints of E_a on their own.

Unlike other intrinsic molecular properties that depend on the structure of a single molecule,¹⁰⁸ enantioselectivity is determined by electronic and/or steric effects stabilising or destabilising one enantiomeric TS to a greater or lesser degree than the other. In that sense, it is to be expected that our target accuracy for E_a , well below 1 kcal mol⁻¹, cannot be reached using only one structure that does not adequately describe the stereocontrolling transition state as an input. To improve the model performance, an alternative representation is



constructed by comparing the representations of both intermediates. Knowing that neither the structure of 2 or 3 are uniquely related to the corresponding activation energies, we can generate such a “reaction-based” representation that draws information from both structures, subtracting the global SLATM of 2 from 3. This is reminiscent of binary reaction fingerprints (obtained by subtracting the products’ from the reactants’ RDKit⁴⁶ fingerprints), which reflect changes in molecular features over reaction processes.¹¹³ The resulting representation (denoted SLATM_{DIFF}) accounts for the differences between the two intermediates and is thus more sensitive to the structural changes occurring during the enantioselective step. By subtracting “reactant” from “product”, the global features that do not change during the catalytic cycle step are eliminated from the representation, and the structural changes between intermediates are highlighted. In this way, we obtain a more faithful representation of the reaction step, which corresponds to a more unique fingerprint of E_a . Although the construction of SLATM_{DIFF} requires the SLATM representations of both intermediates (2 and 3), the computational cost associated with its generation is negligible.

As depicted in the dissimilarity plot (Fig. 1b, middle), the reaction-based representation (SLATM_{DIFF}) is significantly better than SLATM₂: the difference in E_a values tends to zero as the Euclidean distance between their representations tends to zero. In line with this observation, the learning curve (shown by the orange line in Fig. 1a) is significantly improved. The MAE of SLATM_{DIFF} is reduced to 0.31 ± 0.2 kcal mol⁻¹, roughly 50% better than SLATM₂ and up to 60% better than that of SLATM₃ using 90% of the data for training (*i.e.*, 680 structures) in the train/test splits of the cross-validation scheme. Given the rationality of the approach leading to the construction of SLATM_{DIFF}, its gain in accuracy is encouraging. As shown in Fig. 2 and 3, the halved MAE leads to a very notable improvement in the prediction of *e.e.* values. Nevertheless, we note again that very small errors in E_a are amplified when *e.e.* values are calculated, and therefore even a small accuracy gain can be significant.

The high probability density of normalised Euclidean distances between 0.5 and 0.75 seen in Fig. 1b (middle, SLATM_{DIFF}) indicates that the shape adopted by the dissimilarity histogram of SLATM_{DIFF} is not yet ideal, and that further improvement is possible. To achieve higher accuracy, we focus on improving the shape of this dissimilarity plot. Notice that in our ML model, the Euclidean distance is used as a measure of similarity between representations. This means that features with high variance (*i.e.*, that change the most between molecules) dominate the notion of similarity, as they contribute the most to the Euclidean distance between representations. By feature, we mean each of the terms in the molecular representation, which, for SLATM, consist of two- (London dispersion) and three- (Axilrod–Teller–Muto) body potentials computed on groups of atoms closer than a certain cut-off (here, 4.8 Å). The results of these potentials are averaged over their atom-type sets (*e.g.*, all C–C interactions for the two-body terms, all the C–C–C for the three-body terms), which are then concatenated to generate the SLATM vector. The size of the SLATM

representation depends on the existing atom-type sets in the database. Given that our dataset contains the elements C, H, O, N, F, Cl and Si, the total number of features of the SLATM representations is 27 827.

In SLATM_{DIFF}, features with high variance dominate the notion of similarity, measured through the Euclidean distance. However, we are using SLATM to predict a property that is very different from the single-molecule properties for which it was originally designed. Consequently, features with high variance in SLATM are not necessarily the most important fingerprints of E_a . In pursuit of the best possible fingerprint of the activation energy, we assign importance scores to each feature and attempt to focus on the most relevant ones. The linear correlation coefficient (r^2) between each feature and the target property is used as an estimate of the importance of the different terms in the representation. The results, presented in Fig. 4, show that in SLATM_{DIFF} there are only a few high-variance features, while the computed importance scores are spread over many other features that have relatively small variances. Simply put, the variances in the features of the SLATM_{DIFF} representation are not well correlated with their real importance in this application.

Based on this observation, an improved representation, labelled SLATM_{DIFF+}, is generated by selecting only the N_f most important features of SLATM_{DIFF} (specifically, $N_f = 500$) and discarding the rest. This feature selection was done using only the training data at each train/test split of the cross-validation step, as otherwise it could lead to severe overfitting. Nevertheless, the importance scores were consistent across the cross-validation splits thanks to the robustness of the linear regressions. An improved relationship between representation and target distances (Fig. 1b, right) is obtained with the SLATM_{DIFF+} representation, in spite of its reduced size. This simple feature selection leads to a noticeable improvement in accuracy, with a cross-validated MAE of 0.25 ± 0.4 kcal mol⁻¹ (see the green curve in Fig. 1a). Using the SLATM_{DIFF+} representation, the resulting cross-validated correlation coefficients for the

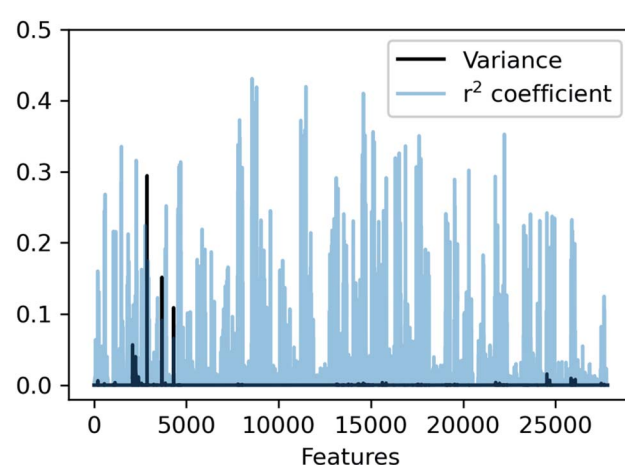


Fig. 4 Variance and correlation coefficient with the target value for each of the 27 827 features of the SLATM_{DIFF} representation in the dataset.



difference between (*R*)- and (*S*)-activation energies ($\Delta\Delta E^\ddagger$, Fig. 2) in the test set are greatly improved ($r^2 > 0.95$). The quality of our fitted model far supersedes previously reported approaches. Good qualitative and even quantitative agreement is achieved between predicted and reference e.e. values computed using the test data splits from the cross-validation runs (Fig. 3).

Since linear correlation constitutes a very limited notion of relevance, other methods, such as nonlinear mutual information criteria,¹¹⁴ were tested as feature importance estimators, but the resulting models showed similar or even worse performance (see the ESI†). Similarly, methods based on metric learning^{111,115} did not lead to any improvement, as the high dimensionality of the problem led to severe overfitting. Ceriotti *et al.*¹¹⁶ suggested the use of principal covariates regression (PCovR) to solve similar issues.¹¹⁷ PCovR is a supervised feature selection method that interpolates between principal component analysis (PCA) and linear regression. Herein, because the variance of the features is completely unrelated to the importance scores, the addition of PCA would not offer any advantage. Nevertheless, these findings highlight the importance of adapting molecular representations to the application at hand, while still preserving the overall generality of the approach.

Chemical insight on asymmetric propargylation catalysts

The ML model is able to reproduce the main trends in e.e. observed across the different catalysts from the 100 different random train/test splits (Fig. 3, top left table). For example, using $\text{SLATM}_{\text{DIFF}^+}$ (Fig. 3, bottom right table), which gives the best predictions with respect to the reference data, catalysts built on scaffold **4** (Scheme 1) are revealed to be outliers, yielding e.e.'s that are significantly different to those obtained with other scaffolds, for a given substituent **a–j**. This is due to the different placement of the substituent *X* on the organocatalysts' scaffold. Excluding **4**, the effect of different substituents on the e.e. is qualitatively the same across all scaffolds, with the exception of **f** ('Pr) and **j** (Ph). The introduction of a phenyl group on the organocatalysts' scaffold leads to highly varied e.e. values, from -97 (*S*) to 91 (*R*). This variation, which is due to the presence of favourable π -stacking and CH/π interactions stabilising some (*S*)-TSs and degrading the enantioselectivity,⁷⁴ is nicely captured by $\text{SLATM}_{\text{DIFF}^+}$. Overall, the high enantioselectivity displayed by (most) catalysts in the library can be attributed to the favourable electrostatic interaction between the formyl C–H of benzaldehyde and one of the chlorines bound to Si, which is present in the lowest-lying (*R*)-ligand arrangement, and absent in the (*S*)-structures.⁷⁴

In their computational screening with AARON,⁷⁴ Wheeler and co-workers identified derivatives of **6** as promising candidates for propargylation reactions. However, these catalysts are difficult to synthesize stereoselectively.^{81,118} Recently, Malkov *et al.* reported the synthesis of a set of terpene-derived atropisomeric bipyridine *N,N'*-dioxides **7** (Fig. 5) as easily-separated diastereoisomers.¹¹⁹ Aromatically-substituted catalysts **7j** and **7k** were shown to be highly active and selective (e.e. of 96 and 97, respectively); additionally, the TS structures for **7** were computationally shown to be nearly identical to the

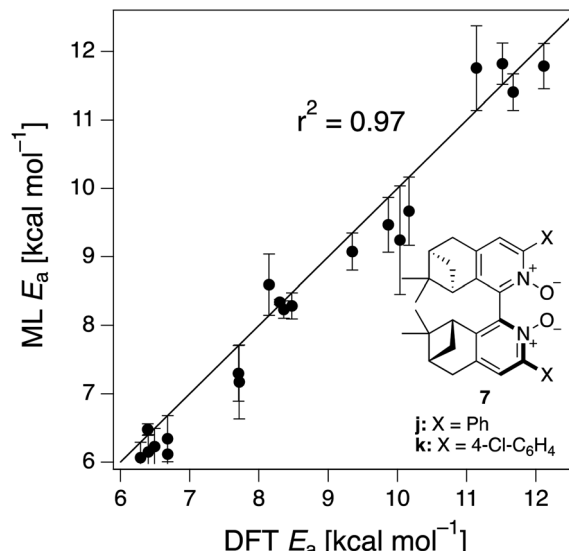


Fig. 5 Out-of-sample predictions on terpene-derived atropisomeric organocatalysts **7j** and **7k**. 10 distinct TSs were computed for each catalyst (BP1–5, (*R*)- and (*S*)-). The error bars are the standard deviation of the 100 predictions from each trained model from the cross-validation scheme.

corresponding substituted forms of **6**.¹¹⁹ Prompted by these results, we decided to test the ML model with $\text{SLATM}_{\text{DIFF}^+}$ to predict the activation energy of the 10 distinct ligand arrangements afforded by **7j** and **7k**. The out-of-sample results are shown in Fig. 5. Despite scaffold **7** and substituent **k** not being in the original training set, excellent correlation between predicted and reference E_a values is obtained ($r^2 = 0.97$). Thus, the enantioselectivity of these out-of-sample catalysts is qualitatively reproduced, despite not achieving exact quantitative agreement between DFT and ML predicted $\Delta\Delta E^\ddagger$ values (1.2 and 1.3 for **7j** and **7k**, respectively, *vs.* 0.2 and 0.5 kcal mol^{-1}).

In summary, we provide a logical route to improve atomistic ML methods for enantioselectivity prediction of asymmetric catalytic reactions, which are limited by both the required accuracy and the small amount of data generally available. Firstly, the intermediates associated with the enantiodetermining step (2 and 3 in Scheme 2) must be identified, and their SLATM representations generated. Secondly, using the difference between the two SLATM representations ($\text{SLATM}_{\text{DIFF}}$) as input, a set of features that map the activation energy accurately can be obtained. Finally, feature engineering can be used to improve $\text{SLATM}_{\text{DIFF}}$, keeping only the most relevant features that relate to the target property. The results show that the ML workflow presented herein is able to accurately predict enantioselectivity from the molecular structures of catalytic cycle intermediates.

Conclusions

In this work, we have developed an atomistic machine learning model to predict the DFT-computed e.e. of Lewis base-catalysed propargylation reactions (Scheme 2). The use of dissimilarity



plots allowed us to rationally develop and progressively improve a reaction-based representation that can be adequately mapped onto the activation energy of the stereocontrolling step. We identified two fundamental limitations of many standard physics-based molecular representations for subtle catalytic properties. First, we have shown that neither the structure of the preceding nor that of the following catalytic cycle intermediate is a fine fingerprint of the energy of the stereocontrolling transition state. This issue can be circumvented by using a reaction-based molecular representation derived from both structures. Finally, we have demonstrated how feature selection can be used to fine-tune this representation.

The resulting model can accurately predict the DFT-computed enantioselectivity of asymmetric propargylations from the structure of catalytic cycle intermediates. Thus, it constitutes a valuable tool to quickly identify potentially selective propargylation organocatalysts. By design, the model is well-balanced between computational cost, generality and accuracy. It is easy to implement for a wide region of chemical space and seamlessly compatible with experimental (e.g., X-ray structures of stable intermediates) and computational data alike. Our results prove that semi-quantitative predictions of e.e. values in asymmetric catalysis can be achieved by accurately predicting E_a .

We conclude that atomistic ML models with adequately tailored molecular representations can be a practical and accurate alternative to both traditional quantum chemical computations of relative rate constants and multivariate linear regression with physical organic molecular descriptors. The stepwise improvement to the model described in this work opens the door to more complex reaction-based and catalytic cycle-based representations. Indeed, ensemble representations, which were recently introduced for properties very sensitive to conformational freedom, such as the free energy of solvation ΔG_{sol} ,¹⁰⁸ are a promising path to go beyond the single structure-to-property paradigm and allow for further generalisation, once combined with the approach discussed herein. Such methodologies will be explored in future work for the accurate screening of enantioselective catalysts in asymmetric reactions.

Author contributions

S. G. performed DFT computations and analyzed the results. R. F. trained and improved the ML models. S. G. and R. F. jointly wrote the manuscript with help from R. L. M. D. W. and R. L. provided feedback on the DFT and ML components, respectively. S. B. and M. D. W. ran preliminary computations initiating this work. All authors discussed the results and commented on the manuscript. C. C. conceived the project with M. D. W., provided supervision and wrote the final version of the manuscript.

Conflicts of interest

There are no conflicts to declare.

Acknowledgements

The authors are grateful to the EPFL for financial support. S. G., R. F. and C. C. acknowledge funding from the European Research Council (ERC, Grant Agreement No. 817977) within the framework of European Union's H2020. The National Centre of Competence in Research (NCCR) "Sustainable chemical process through catalysis (Catalysis)" of the Swiss National Science Foundation (SNSF) is acknowledged for financial support of R. L. S. B. acknowledges the NCCR "Materials' Revolution: Computational Design and Discovery of Novel Materials (MARVEL)" for providing a "INSPIRE" master fellowship. The authors thank Benjamin Meyer for helpful discussions at the origin of the project.

References

- 1 M. S. Taylor and E. N. Jacobsen, *Proc. Natl. Acad. Sci. U. S. A.*, 2004, **101**, 5368–5373.
- 2 R. E. Gawley and J. Aubé, in *Principles of Asymmetric Synthesis*, ed. R. E. Gawley and J. Aubé, Elsevier, Oxford, 2nd edn, 2012, pp. 63–95.
- 3 D. W. C. MacMillan, *Nature*, 2008, **455**, 304–308.
- 4 P. I. Dalko and L. Moisan, *Angew. Chem., Int. Ed.*, 2001, **40**, 3726–3748.
- 5 P. I. Dalko, in *Enantioselective Organocatalysis*, John Wiley & Sons, Ltd, 2007, pp. 1–17.
- 6 S.-H. Xiang and B. Tan, *Nat. Commun.*, 2020, **11**, 3786.
- 7 C. Poree and F. Schoenebeck, *Acc. Chem. Res.*, 2017, **50**, 605–608.
- 8 K. N. Houk and F. Liu, *Acc. Chem. Res.*, 2017, **50**, 539–543.
- 9 S. E. Wheeler, T. J. Seguin, Y. Guan and A. C. Doney, *Acc. Chem. Res.*, 2016, **49**, 1061–1069.
- 10 Q. Peng, F. Duarte and R. S. Paton, *Chem. Soc. Rev.*, 2016, **45**, 6093–6107.
- 11 E. Hansen, A. R. Rosales, B. Tutkowska, P.-O. Norrby and O. Wiest, *Acc. Chem. Res.*, 2016, **49**, 996–1005.
- 12 K. H. Hopmann, *Int. J. Quantum Chem.*, 2015, **115**, 1232–1249.
- 13 A. S. K. Tsang, I. A. Sanhueza and F. Schoenebeck, *Chem.–Eur. J.*, 2014, **20**, 16432–16441.
- 14 D. Sepúlveda, T. Lu and S. E. Wheeler, *Org. Biomol. Chem.*, 2014, **12**, 8346–8353.
- 15 D. Balcells, E. Clot, O. Eisenstein, A. Nova and L. Perrin, *Acc. Chem. Res.*, 2016, **49**, 1070–1078.
- 16 P. H. Cheong, C. Y. Legault, J. M. Um, N. Celebi-Olcum and K. N. Houk, *Chem. Rev.*, 2011, **111**, 5042–5137.
- 17 T. Sperger, I. A. Sanhueza, I. Kalvet and F. Schoenebeck, *Chem. Rev.*, 2015, **115**, 9532–9586.
- 18 M. Foscato and V. R. Jensen, *ACS Catal.*, 2020, **10**, 2354–2377.
- 19 V. M. Ingman, A. J. Schaefer, L. R. Andreola and S. E. Wheeler, *Wiley Interdiscip. Rev.: Comput. Mol. Sci.*, 2020, e1510.
- 20 Y. Guan, V. M. Ingman, B. J. Rooks and S. E. Wheeler, *J. Chem. Theory Comput.*, 2018, **14**, 5249–5261.
- 21 A. R. Rosales, J. Wahlers, E. Limé, R. E. Meadows, K. W. Leslie, R. Savin, F. Bell, E. Hansen, P. Helquist,

R. H. Munday, O. Wiest and P.-O. Norrby, *Nat. Catal.*, 2019, **2**, 41–45.

22 J. D. Oslob, B. Åkermark, P. Helquist and P. O. Norrby, *Organometallics*, 1997, **16**, 3015–3021.

23 K. B. Lipkowitz and M. Pradhan, *J. Org. Chem.*, 2003, **68**, 4648–4656.

24 K. C. Harper and M. S. Sigman, *Science*, 2011, **333**, 1875.

25 M. S. Sigman, K. C. Harper, E. N. Bess and A. Milo, *Acc. Chem. Res.*, 2016, **49**, 1292–1301.

26 J. P. Reid and M. S. Sigman, *Nat. Rev. Chem.*, 2018, **2**, 290–305.

27 $\Delta\Delta G^\ddagger$, calculated from the experimental enantioselectivity using Gibbs's free energy equation ($\Delta\Delta G^\ddagger = -RT \ln|\text{e.r.}|$, e.r. = enantiomeric ratio).

28 K. C. Harper and M. S. Sigman, *J. Org. Chem.*, 2013, **78**, 2813–2818.

29 C. B. Santiago, J. Y. Guo and M. S. Sigman, *Chem. Sci.*, 2018, **9**, 2398–2412.

30 D. J. Durand and N. Fey, *Chem. Rev.*, 2019, **119**, 6561–6594.

31 A. Milo, E. N. Bess and M. S. Sigman, *Nature*, 2014, **507**, 210–214.

32 S. E. Denmark, N. D. Gould and L. M. Wolf, *J. Org. Chem.*, 2011, **76**, 4337–4357.

33 A. Milo, A. J. Neel, F. D. Toste and M. S. Sigman, *Science*, 2015, **347**, 737.

34 E. N. Bess, A. J. Bischoff and M. S. Sigman, *Proc. Natl. Acad. Sci. U. S. A.*, 2014, **111**, 14698.

35 J. Werth and M. S. Sigman, *J. Am. Chem. Soc.*, 2020, **142**, 16382–16391.

36 J. P. Reid and M. S. Sigman, *Nature*, 2019, **571**, 343–348.

37 A. F. Zahrt, S. V. Athavale and S. E. Denmark, *Chem. Rev.*, 2020, **120**, 1620–1689.

38 J. B. O. Mitchell, *Wiley Interdiscip. Rev.: Comput. Mol. Sci.*, 2014, **4**, 468–481.

39 I. Funes-Ardoiz and F. Schoenebeck, *Chem.*, 2020, **6**, 1904–1913.

40 J. R. Kitchin, *Nat. Catal.*, 2018, **1**, 230–232.

41 W. Yang, T. T. Fidelis and W.-H. Sun, *ACS Omega*, 2020, **5**, 83–88.

42 Z. Li, S. Wang and H. Xin, *Nat. Catal.*, 2018, **1**, 641–642.

43 B. Meyer, B. Sawatlon, S. Heinen, O. A. von Lilienfeld and C. Corminboeuf, *Chem. Sci.*, 2018, **9**, 7069–7077.

44 M. Cordova, M. D. Wodrich, B. Meyer, B. Sawatlon and C. Corminboeuf, *ACS Catal.*, 2020, **10**, 7021–7031.

45 M. D. Wodrich, A. Fabrizio, B. Meyer and C. Corminboeuf, *Chem. Sci.*, 2020, **11**, 12070–12080.

46 RDKit: open-source chemoinformatics and machine learning, <http://www.rdkit.org>.

47 A. F. Zahrt, J. J. Henle, B. T. Rose, Y. Wang, W. T. Darrow and S. E. Denmark, *Science*, 2019, **363**, eaau5631.

48 J. J. Henle, A. F. Zahrt, B. T. Rose, W. T. Darrow, Y. Wang and S. E. Denmark, *J. Am. Chem. Soc.*, 2020, **142**, 11578–11592.

49 A. Tomberg, M. J. Johansson and P.-O. Norrby, *J. Org. Chem.*, 2019, **84**, 4695–4703.

50 S. Singh, M. Pareek, A. Changotra, S. Banerjee, B. Bhaskararao, P. Balamurugan and R. B. Sunoj, *Proc. Natl. Acad. Sci. U. S. A.*, 2020, **117**, 1339–1345.

51 J. Chen, W. Jiwu, L. Mingzong and T. You, *J. Mol. Catal. A: Chem.*, 2006, **258**, 191–197.

52 Y. Amar, A. M. Schweidtmann, P. Deutsch, L. Cao and A. Lapkin, *Chem. Sci.*, 2019, **10**, 6697–6706.

53 S. Banerjee, A. Sreenithya and R. B. Sunoj, *Phys. Chem. Chem. Phys.*, 2018, **20**, 18311–18318.

54 W. Beker, E. P. Gajewska, T. Badowski and B. A. Grzybowski, *Angew. Chem., Int. Ed.*, 2019, **58**, 4515–4519.

55 S. M. Maley, D.-H. Kwon, N. Rollins, J. C. Stanley, O. L. Sydora, S. M. Bischof and D. H. Ess, *Chem. Sci.*, 2020, **11**, 9665–9674.

56 V. Dhayalan, S. C. Gadekar, Z. Alassad and A. Milo, *Nat. Chem.*, 2019, **11**, 543–551.

57 D. T. Ahneman, J. G. Estrada, S. Lin, S. D. Dreher and A. G. Doyle, *Science*, 2018, **360**, 186.

58 M. K. Nielsen, D. T. Ahneman, O. Riera and A. G. Doyle, *J. Am. Chem. Soc.*, 2018, **140**, 5004–5008.

59 K. Jorner, T. Brinck, P.-O. Norrby and D. Buttar, *Chem. Sci.*, 2021, **12**, 1163–1175.

60 F. Sandfort, F. Strieth-Kalthoff, M. Kühnemund, C. Beecks and F. Glorius, *Chem.*, 2020, **6**, 1379–1390.

61 J. M. Granda, L. Donina, V. Dragone, D.-L. Long and L. Cronin, *Nature*, 2018, **559**, 377–381.

62 C. W. Coley, W. Jin, L. Rogers, T. F. Jamison, T. S. Jaakkola, W. H. Green, R. Barzilay and K. F. Jensen, *Chem. Sci.*, 2019, **10**, 370–377.

63 P. Friederich, G. dos Passos Gomes, R. De Bin, A. Aspuru-Guzik and D. Balcells, *Chem. Sci.*, 2020, **11**, 4584–4601.

64 S. Heinen, G. F. von Rudorff and O. A. von Lilienfeld, [arXiv:2009.13429](https://arxiv.org/abs/2009.13429), 2020.

65 G. F. von Rudorff, S. N. Heinen, M. Bragato and O. A. von Lilienfeld, [arXiv:2006.00504](https://arxiv.org/abs/2006.00504), 2020.

66 M. Bragato, G. F. von Rudorff and O. A. von Lilienfeld, *Chem. Sci.*, 2020, **11**, 11859–11868.

67 G. Skoraczyński, P. Dittwald, B. Miasojedow, S. Szymkuć, E. P. Gajewska, B. A. Grzybowski and A. Gambin, *Sci. Rep.*, 2017, **7**, 3582.

68 M. Rupp, A. Tkatchenko, K.-R. Müller and O. A. von Lilienfeld, *Phys. Rev. Lett.*, 2012, **108**, 058301.

69 B. Huang and O. A. von Lilienfeld, *Nat. Chem.*, 2020, **12**, 945–951.

70 S. De, A. P. Bartók, G. Csányi and M. Ceriotti, *Phys. Chem. Chem. Phys.*, 2016, **18**, 13754–13769.

71 O. A. von Lilienfeld, K.-R. Müller and A. Tkatchenko, *Nat. Rev. Chem.*, 2020, **4**, 347–358.

72 O. A. von Lilienfeld and K. Burke, *Nat. Commun.*, 2020, **11**, 4895.

73 X. Li, S. Q. Zhang, L. C. Xu and X. Hong, *Angew. Chem., Int. Ed.*, 2020, **59**, 13253–13259.

74 A. C. Doney, B. J. Rooks, T. Lu and S. E. Wheeler, *ACS Catal.*, 2016, **6**, 7948–7955.

75 S. E. Denmark, D. M. Coe, N. E. Pratt and B. D. Griedel, *J. Org. Chem.*, 1994, **59**, 6161–6163.

76 S. E. Denmark and J. Fu, *J. Am. Chem. Soc.*, 2000, **122**, 12021–12022.

77 S. E. Denmark and T. Wynn, *J. Am. Chem. Soc.*, 2001, **123**, 6199–6200.



78 S. E. Denmark and G. L. Beutner, *Angew. Chem., Int. Ed.*, 2008, **47**, 1560–1638.

79 C.-H. Ding and X.-L. Hou, *Chem. Rev.*, 2011, **111**, 1914–1937.

80 J. A. Marshall, *J. Org. Chem.*, 2007, **72**, 8153–8166.

81 M. Nakajima, M. Saito, M. Shiro and S.-i. Hashimoto, *J. Am. Chem. Soc.*, 1998, **120**, 6419–6420.

82 M. Nakajima, M. Saito and S. Hashimoto, *Tetrahedron: Asymmetry*, 2002, **13**, 2449–2452.

83 J. Chen, B. Captain and N. Takenaka, *Org. Lett.*, 2011, **13**, 1654–1657.

84 T. Lu, M. A. Porterfield and S. E. Wheeler, *Org. Lett.*, 2012, **14**, 5310–5313.

85 B. J. Rooks, M. R. Haas, D. Sepúlveda, T. Lu and S. E. Wheeler, *ACS Catal.*, 2015, **5**, 272–280.

86 T. Lu, R. Zhu, Y. An and S. E. Wheeler, *J. Am. Chem. Soc.*, 2012, **134**, 3095–3102.

87 4 intermediates (1f_S_bp2 int 2, 3e_R_bp1 int 3, 3e_S_bp1 int 3, and 3j_S_bp2 int 3) could not be converged, therefore the corresponding enantiomeric TS structures were removed from the original database of 760 TSs.

88 K. Vu, J. C. Snyder, L. Li, M. Rupp, B. F. Chen, T. Khelif, K.-R. Müller and K. Burke, *Int. J. Quantum Chem.*, 2015, **115**, 1115–1128.

89 K. Hansen, G. Montavon, F. Biegler, S. Fazli, M. Rupp, M. Scheffler, O. A. von Lilienfeld, A. Tkatchenko and K.-R. Müller, *J. Chem. Theory Comput.*, 2013, **9**, 3404–3419.

90 R. Ramakrishnan, P. O. Dral, M. Rupp and O. A. von Lilienfeld, *J. Chem. Theory Comput.*, 2015, **11**, 2087–2096.

91 D. Hu, Y. Xie, X. Li, L. Li and Z. Lan, *J. Phys. Chem. Lett.*, 2018, **9**, 2725–2732.

92 J. Westermayr, F. A. Faber, A. S. Christensen, O. A. von Lilienfeld and P. Marquetand, *Mach. Learn.: Sci. Technol.*, 2020, **1**, 025009.

93 Q. V. Nguyen, S. De, J. Lin and V. Cevher, *Int. J. Quantum Chem.*, 2019, **119**, e25872.

94 S. N. Pozdnyakov, M. J. Willatt, A. P. Bartók, C. Ortner, G. Csányi and M. Ceriotti, *Phys. Rev. Lett.*, 2020, **125**, 166001.

95 R. Tibshirani and J. Friedman, *The Elements of Statistical Learning: Data Mining, Inference, and Prediction*, Springer, 2001.

96 A. D. Becke, *J. Chem. Phys.*, 1997, **107**, 8554–8560.

97 A. Schäfer, C. Huber and R. Ahlrichs, *J. Chem. Phys.*, 1994, **100**, 5829–5835.

98 S. Grimme, *J. Comput. Chem.*, 2006, **27**, 1787–1799.

99 E. Cancès and B. Mennucci, *J. Math. Chem.*, 1998, **23**, 309–326.

100 E. Cancès, B. Mennucci and J. Tomasi, *J. Chem. Phys.*, 1997, **107**, 3032–3041.

101 J. Tomasi, B. Mennucci and R. Cammi, *Chem. Rev.*, 2005, **105**, 2999–3094.

102 M. J. Frisch, G. W. Trucks, H. B. Schlegel, G. E. Scuseria, M. A. Robb, J. R. Cheeseman, G. Scalmani, V. Barone, G. A. Petersson, H. Nakatsuji, X. Li, M. Caricato, A. V. Marenich, J. Bloino, B. G. Janesko, R. Gomperts, B. Mennucci, H. P. Hratchian, J. V. Ortiz, A. F. Izmaylov, J. L. Sonnenberg, D. Williams-Young, F. Ding, F. Lipparini, F. Egidi, J. Goings, B. Peng, A. Petrone, T. Henderson, D. Ranasinghe, V. G. Zakrzewski, J. Gao, N. Rega, G. Zheng, W. Liang, M. Hada, M. Ehara, K. Toyota, R. Fukuda, J. Hasegawa, M. Ishida, T. Nakajima, Y. Honda, O. Kitao, H. Nakai, T. Vreven, K. Throssell, J. A. Jr, J. E. Peralta, F. Ogliaro, M. J. Bearpark, J. J. Heyd, E. N. Brothers, K. N. Kudin, V. N. Staroverov, T. A. Keith, R. Kobayashi, J. Normand, K. Raghavachari, A. P. Rendell, J. C. Burant, S. S. Iyengar, J. Tomasi, M. Cossi, J. M. Millam, M. Klene, C. Adamo, R. Cammi, J. W. Ochterski, R. L. Martin, K. Morokuma, O. Farkas, J. B. Foresman and D. J. Fox, *Gaussian 16 Rev. C.01*, Wallingford, CT, 2016.

103 Because the original TS database was computed with Gaussian09, the fine (75 302) integration grid (default of Gaussian09) was used instead of the ultrafine (99 590) grid (default of Gaussian16).

104 K. Fukui, *Acc. Chem. Res.*, 1981, **14**, 363–368.

105 A. S. Christensen, F. A. Faber, B. Huang, L. A. Bratholm, A. Tkatchenko, K. R. Müller and O. A. von Lilienfeld, *QML : A Python Toolkit for Quantum Machine Learning*, 2017.

106 F. Pedregosa, G. Varoquaux, A. Gramfort, V. Michel, B. Thirion, O. Grisel, M. Blondel, P. Prettenhofer, R. Weiss, V. Dubourg, J. Vanderplas, A. Passos, D. Cournapeau, M. Brucher, M. Perrot and E. Duchesnay, *J. Mach. Learn. Res.*, 2011, **12**, 2825–2830.

107 K. Hansen, F. Biegler, R. Ramakrishnan, W. Pronobis, O. A. von Lilienfeld, K.-R. Müller and A. Tkatchenko, *J. Phys. Chem. Lett.*, 2015, **6**, 2326–2331.

108 J. Weinreich, N. J. Browning and O. A. von Lilienfeld, arXiv:2012.09722, 2020.

109 A. S. Christensen, L. A. Bratholm, F. A. Faber and O. Anatole von Lilienfeld, *J. Chem. Phys.*, 2020, **152**, 044107.

110 F. A. Faber, A. S. Christensen, B. Huang and O. A. von Lilienfeld, *J. Chem. Phys.*, 2018, **148**, 241717.

111 G. S. Na, H. Chang and H. W. Kim, *Phys. Chem. Chem. Phys.*, 2020, **22**, 18526–18535.

112 G. S. Hammond, *J. Am. Chem. Soc.*, 1955, **77**, 334–338.

113 G. Skoraczynski, P. Dittwald, B. Miasojedow, S. Szymkuc, E. P. Gajewska, B. A. Grzybowski and A. Gambin, *Sci. Rep.*, 2017, **7**, 3582.

114 B. C. Ross, *PLoS One*, 2014, **9**, e87357.

115 Q. W. Kilian and T. Gerald, presented in part at the Eleventh International Conference on Artificial Intelligence and Statistics, 2007/03/11, 2007.

116 B. A. Helfrecht, R. K. Cersonsky, G. Fraux and M. Ceriotti, arXiv:2002.05076, 2020.

117 B. A. Helfrecht, R. K. Cersonsky, G. Fraux and M. Ceriotti, *Mach. Learn.: Sci. Technol.*, 2020, **1**, 045021.

118 A. V. Malkov, M.-M. Westwater, A. Gutnov, P. Ramírez-López, F. Friscourt, A. Kadlčíková, J. Hodačová, Z. Rankovic, M. Kotora and P. Kočovský, *Tetrahedron*, 2008, **64**, 11335–11348.

119 V. Y. Vaganov, Y. Fukazawa, N. S. Kondratyev, S. A. Shipilovskikh, S. E. Wheeler, A. E. Rubtsov and A. V. Malkov, *Adv. Synth. Catal.*, 2020, **362**, 5467–5474.

